nature communications

Article

https://doi.org/10.1038/s41467-025-56814-w

An optoelectrochemical synapse based on a single-component n-type mixed conductor

Received: 17 September 2024

Accepted: 30 January 2025

Published online: 13 February 2025

Check for updates

Yazhou Wang[1,6], Wentao Shan[1,6], Hanrui Li[2], Yizhou Zhong[1], Shofarul Wustoni[1], Johana Uribe[1], Tianrui Chang[1], Valentina E. Musteata[3], Tania Cecilia Hidalgo Castillo[1], Wan Yue[4], Haifeng Ling[5], Nazek El-Atab[2] & Sahika Inal[1]

Organic mixed ionic-electronic conductors (OMIECs) are materials that can be used to build bio-inspired electronic devices as they emulate ion-based cellular communication through doping with aqueous ionic charges. The integration of charge photogeneration and electrochemical doping processes in the polymer film enables optoelectronic applications that involve synaptic transistors. However, no OMIEC has yet been implemented to create a miniaturized photoactive platform capable of perceiving and processing multi-spectral visual information. Here, we present a materials and device design concept in which an n-type OMIEC film is incorporated into the micron-scale channel of an electrochemical transistor operating directly in an aqueous electrolyte under ambient conditions. The conjugated polymer channel, consisting of a fluorinated bisistain-lactone-bithiazole acceptor, has a current modulated in response to both electrical and optical stimuli, emulating the multimodal function of the visual nervous system. Our optoelectrochemical synapse achieves multilevel conductance states as well as transduction of visual information covering ultraviolet, visible, and near-infrared regions of the spectrum – a range beyond that of the human visual system's perception. The resulting transistor active-matrix array is capable of adaptive sensing, memory, and pre-processing of visual information, demonstrating an efficient optoelectronic neuromorphic system with multi-task learning capability.

The conversion of external information into biological signals by the sensory nervous system is at the core of how living organisms interact with their environment[1–3]. Receiving the majority of the external information as visual cues, the human visual system is able to recognize and remember the identity of a wide range of objects. The processes in human visual system processes have thus inspired the development of artificial visual systems implemented through electronic devices[4,5]. Optoelectronic synapses have been instrumental in the progression of such neuromorphic devices that can decode images[6–8] or enable artificial vision[9]. However, most optoelectronic devices utilized in hardware

[1]Organic Bioelectronics Laboratory, Biological and Environmental Science and Engineering Division, King Abdullah University of Science and Technology (KAUST), Thuwal 23955-6900, Saudi Arabia. [2]Smart, Advanced Memory Devices and Applications (SAMA) Laboratory, Computer Electrical Mathematical Science and Engineering Division, King Abdullah University of Science and Technology (KAUST), Thuwal 23955-6900, Saudi Arabia. [3]Imaging and Characterization Core Lab, King Abdullah University of Science and Technology (KAUST), Thuwal 23955-6900, Saudi Arabia. [4]School of Materials Science and Engineering, State Key Laboratory of Optoelectronic Materials and Technologies, Key Laboratory for Polymeric Composite and Functional Materials of Ministry of Education, Guangzhou Key Laboratory of Flexible Electronic Materials and Wearable Devices, Sun Yat-sen University, Guangzhou 510275, China. [5]State Key Laboratory of Flexible Electronics (LoFE) & Institute of Advanced Materials (IAM), Nanjing University of Posts & Telecommunications, Nanjing 210023, China. [6]These authors contributed equally: Yazhou Wang, Wentao Shan. e-mail: sahika.inal@kaust.edu.sa

neural networks and neural interfaces are composed of inorganic materials, which are often mechanically hard, not biocompatible and lack additional functionalities. Rendering these devices light responsive requires additional circuit elements whose operational mechanisms are fundamentally different than those found in biological systems[10].

Organic mixed ionic-electronic charge conductors (OMIECs) are ideal electronic materials for developing artificial circuits as they can emulate the ion-mediated mechanisms of biological synapses[11–16]. OMIECs are soft conjugated polymers that exhibit volumetric ionic and electronic charge transport in their films with often compatibility with living systems. Organic electrochemical transistors (OECTs) leverage the mixed conductivity of OMIECs by incorporating their solution-processed films in microscale channels and translating ionic, biological information in aqueous media into amplified electronic signals[17,18]. The OMIEC channel achieves multiple, distinct doping states through small ionic fluxes in the electrolyte, generating high device transconductance at low operating voltages (<1 V)[19–21]. OECTs have been shown to exhibit both long-term and short-term plasticity behavior, with high potential for integration as artificial synapses[22,23].

For neuromorphic vision engineering, OMIECs feature one crucial property that has yet to be exploited: the ability to absorb light[24,25]. A few recent reports have demonstrated the application of OECTs as optoelectronic synapses converting light-based signals into spike-train signal patterns[26]. However, these studies do not leverage the light sensitivity of OMIECs in the channel but rather depend on light-sensitive materials integrated into large-area gate electrodes[25,27], rendering these systems difficult to operate, miniaturize, and integrate. The only demonstration of a miniaturized OECT-based optoelectronic synapse, which generated a non-volatile light-induced memory, used conventional organic semiconductors[10] (a bi-component donor/acceptor system, P3HT:PCBM), in the channel, which are not compatible with aqueous electrolytes and require a toxic ionic liquid as the electrolyte. Moreover, while current organic synaptic transistors have demonstrated light signal processing capability, they can process information at only one wavelength or a restricted range of wavelengths[28–30]. Furthermore, mimicking the human visual system demands multifunctional materials that are responsive to both light and electrical stimuli, as visual memory and recognition rely on photoreceptor cells that capture visual information and afferent neurons that transmit this input as electrical signals. Thus, to build a biomimetic optoelectronic synapse, the development of multi-stimuli-responsive OMIECs with the ability to perceive multispectral visual information is key to surpassing the functionality of single-mode (electric or optical) drives[31].

Here we develop an organic ion-tunable optoelectrochemical synapse by using a single-component OMIEC as the OECT channel that responds to both light and voltage stimuli applied through an aqueous electrolyte (Fig. 1a). The OMIEC we designed is an n-type, all electron-accepting copolymer consisting of bisistain-lactone and bithiazole (p(C2F-z)) (Fig. 1b), synthesized through the green Aldol polymerization technique. Our synapse demonstrates multispectral visual perception covering a broad wavelength range (ultraviolet, visible, and near-infrared regions), even beyond the perception range of the human visual system. Our single-component material is responsive not only to optical stimuli but also to electrical input, further mimicking the electrical transmission in the retina. The optoelectrochemical synapse emulates the functionality of a biological synapse such as synaptic plasticity and pair-pulse facilitation, and it exhibits the transition of a short-term memory to a long-term memory at low programming voltages (0.4 V), emulating the learning experience of the brain. Through a combination of in situ and ex situ optoelectrochemical methods, we investigate the working mechanism of these devices, which relies on the light-induced aqueous ion-based doping of the channel, with the extent precisely controlled by the training pattern. By building a synaptic array based on an 8 × 8 array of these devices on a 9.4 × 6.6 mm^2 area, we show this aquoues electrolyte compatible device's capability for image recognition, preprocessing, and memory. In addition, we demonstrate the use of our device for in-sensor reservoir computing and full-color image processing, highlighting its capability for decoding multitask spatiotemporal events and extracting color information in biological media. Lastly, our synaptic device performs temporal summation under high-frequency electrical pulses, which we leverage for motion recognition.

Results and discussion

Polymer design and OECT performance

We designed an oligo(ethylene glycol)-functionalized lactone-based polymer as an OECT channel material, considering the favorable charge transport characteristics of this class of OMIECs[32–34]. The polymer, p(C2F-z), comprises all electron-accepting building blocks, namely fluorinated bisistain-lactone and bithiazole, and was synthesized using Aldol polymerization to achieve a number-average molecular weights of 97.0 kDa and weight-average molecular weight of 144.7 kDa (Section 1. Synthetic Procedures in supplementary information and Figs. S1–6). The dual electron-deficient acceptor unit leads to a deep-lying lowest unoccupied molecular orbital (LUMO) of −4.49 eV (see Fig. S7 for the LUMO determination). This semiconducting film has a pseudo-capacitive-like charging behavior with a reduction onset of ca. 0.2 V in aqueous NaCl solution (Fig. S8a) and a wide-range absorption across the ultraviolet, visible, and near-infrared spectra (Fig. S8b). In situ UV-VIS-NIR spectrochemistry, ex situ X-ray photoelectron spectroscopy, and quartz crystal microbalance with dissipation monitoring studies evidence the ingress of Na^+ in the bulk of the film upon application of doping voltages higher than 0.2 V vs. Ag/AgCl and the subsequent formation of polaronic species (Fig. S8c–e). The solution-processed films form smooth, well-adhering layers on metals such as Au with a thickness of 80–100 nm (Fig. S8f).

Confirming that this polymer is able to undergo reversible volumetric charging with water-based ions and has a low onset of reduction, we spin-coated it onto OECT channels with a width of 100 µm and length of 10 µm, patterned using photolithography (Fig. 1b). To characterize the performance of this new polymer in OECTs and benchmark its mixed conduction properties, we used an Ag/AgCl pellet as the gate electrode. The devices were operated in a 0.1 M NaCl solution with gate voltages (V_G) between 0-0.6 V applied with respect to the source contact. Figure 1c shows the transfer and transconductance characteristics of p(C2F-z) OECTs, demonstrating typical n-type enhancement-mode transistor behavior (see output curves in Fig. S9c). The device performance figures of merits are summarized in Table S1. The p(C2F-z) OECT exhibits a turn-on at a very low voltage (threshold voltage, V_{TH} = 0.07 V, Fig. S10a), correlated with its low-lying LUMO level. At V_D = 0.6 V and V_G = 0.45 V, the maximum geometry-normalized transconductance ($g_{m,n}$) reaches 25.94 S cm^{-1} with drain current (I_D) of few sub mA. The product of electron mobility and volumetric capacitance (µC*) value, used to benchmark the material's mixed conduction performance, is extracted from the slope of the linear fit to the corresponding plot of g_m versus $(Wd/L)(V_G-V_{TH})$ and as high as 84.65 F V^{-1} cm^{-1} s^{-1}. The C^* was determined to be 81 F cm^{-3} using electrochemical impedance spectroscopy (Fig. S10b–d). The µ is 1.04 $cm^2 V^{-1}$ s^{-1}, a record-high electron mobility ever measured from OECTs (Fig. 1d and Table S2). The low V_{TH}, along with the high carrier mobility, makes p(C2F-z) a promising potential for building synapses with low power demand. The high mobility allows a fast-switching speed of τ_{ON}/τ_{OFF} = 365 µs /71 µs (Fig. 1e). These features are accompanied by high operational stability (Fig. 1f), with the device exhibiting a channel current maintaining 93% of its channel current after 1 h of continuous doping/dedoping cycles.

Optoelectrochemical synapse characteristics

The p(C2F-z) OECT exhibits excellent ionic-electronic signal transduction performance, a fast response time, a low operating voltage,

and high stability operation in aqueous media under ambient conditions. For optoelectronic applications, the device needs to show a response to light, and no OMIEC channel with a conventional gate, such as an Au electrode, has yet been reported to show currents scaling with light intensity in an aqueous electrolyte. To assess the p(C2F-z) OECT response to light, we recorded the transfer curves in the dark and under continuous exposure to a 375 nm light source. The measurements were conducted while exposing the channel to different light intensities and using a planar Au gold electrode as the gate electrode and 0.1 M NaCl as the electrolyte (Fig. S11a). In the dark conditions, this device displayed a threshold voltage of 0.13 V and an I_{ON}/I_{OFF} ratio of 4.76×10^5. Upon illumination at a power of 200 mW cm^{-2}, the threshold voltage shifted to −0.18 V, and the I_{ON}/I_{OFF} ratio reached 1.52×10^3. The illumination shifted the transfer curve upward with a gradual increase in the channel current proportional to the light intensity (Fig. 2a). Remarkably, the light-gated device achieved current values that surpass those attainable through electrochemical doping alone. When the film was used as an electrode, its current measured with respect to a reference electrode also increased with an increase in the intensity of the light, suggesting that the photocurrents measured originate from the film alone (Fig. S11b–f).

Next, we proceeded to investigate the fundamental characteristics of the optoelectrochemical synapse. The synaptic weight, representing the strength of the connection between the pre-synapse and post-synapse, was examined. We considered the light pulse as the presynaptic stimulus, and the resulting photoresponse represented the synaptic weight in the form of post-synaptic current (I_D). Upon applying light pulses with a width of 0.1 s and an off length of 0.05 s, we observed a substantial increase in channel current, followed by a gradual decrease as the light source was removed (Fig. 2b). This light-based training enabled the generation of 512 distinct linear conductance states, demonstrating an ultrahigh 9-bit state of optical

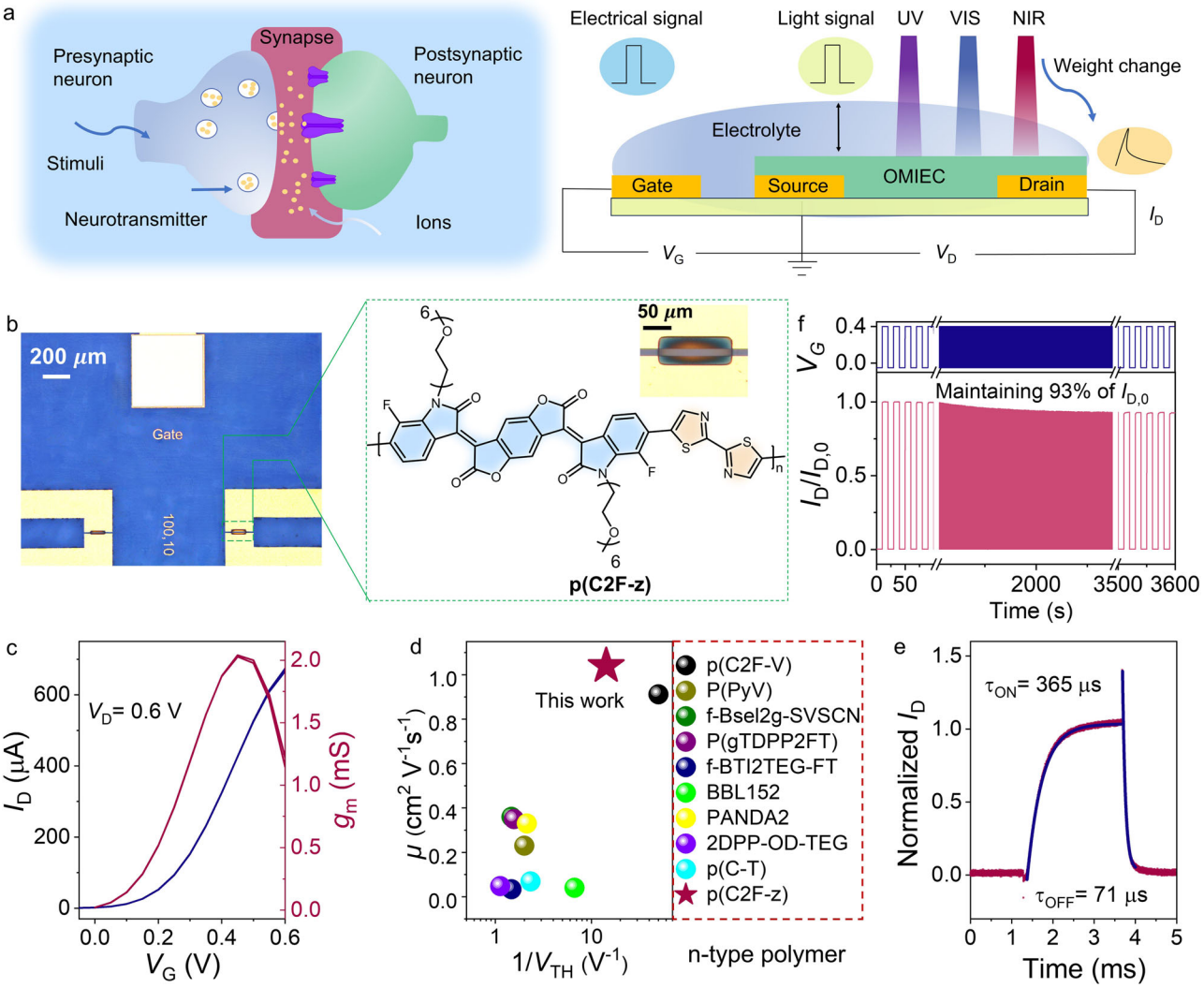

Fig. 1 | Optoelectrochemical synapse based on an n-type organic electrochemical transistor. Schematic illustrations of (**a**) a biological synapse (left) and our transistor design that acts as an ion-tunable optoelectrochemical synapse (right). In the human visual system, communication between neurons occurs through synapses. The stimulation of the presynaptic membrane generates an action potential that results in the flow of ions towards the postsynaptic neuron. The OECT based synapse mimics this function by responding to external optical and electrical signals and converting them into a frequency encoded current output. In synapses, synaptic weight is responsible for learning and storing visual information and memory. **b** Chemical structure of p(C2F-z) with the microscope image of its film in the microscale OECT channel (length = 10 μm, width = 100 μm, d = 79 nm) and the lateral Au gate electrode. The schematic representation and a microscope image of the OECT are shown in Fig. S9a, b. **c** The transfer (I_D–V_G) and transconductance (g_m–V_G) characteristics of the p(C2F-z) OECT. V_D = 0.6 V. **d** Comparison of p(C2F-z) device performance metrics (μ and V_{TH}) with those of other high-performance n-type OECTs. **e** Transient characteristics of p(C2F-z) OECT. The blue lines show the exponential fit with the corresponding turn ON and OFF speeds (τ_{ON} and τ_{OFF}). **f** The operational stability of a p(C2F-z) OECT. V_G pulses of 0.4 V with 10 s ON and 10 s OFF were applied for 3600 s at V_D = 0.5 V. All device characteristics were recorded with an Ag/AgCl reference electrode used as the gate.

https://doi.org/10.1038/s41467-025-56814-w

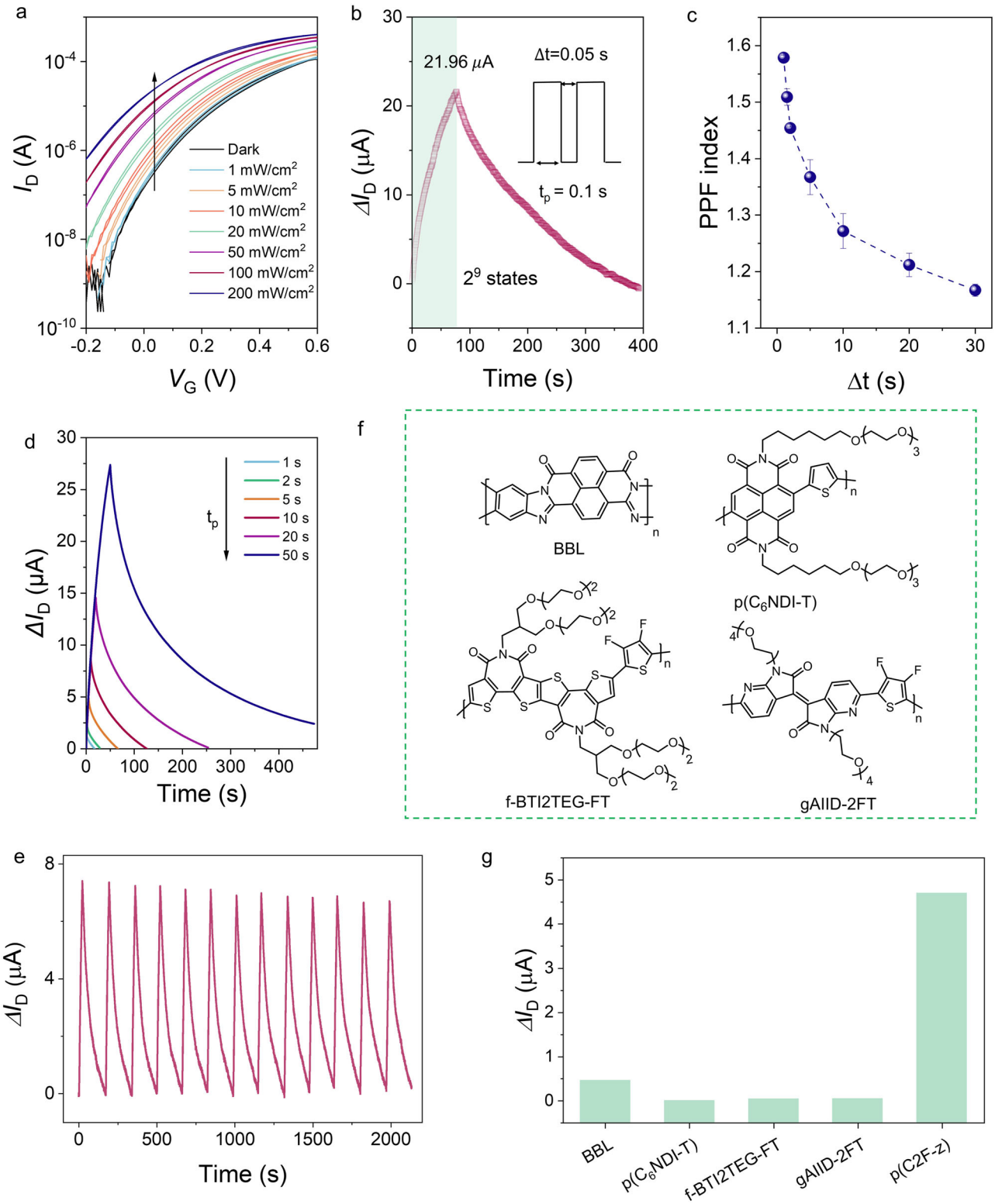

Fig. 2 | The optical response of the n-type organic optoelectrochemical transistor. a Transfer characteristics measured in the dark and at various light intensities (λ = 375 nm) at V_D = 0.4 V. **b** The device current change as a function of time as the device was modulated with 512 light pulses, and the current was spontaneously erased. The light intensity was 200 mW cm^{-2}, the pulse width (t_p) was 0.1 s with the pulse interval (Δt) of 0.05 s and $V_D = V_G$ = 0.4 V. **c** PPF index as a function of pulse interval time with a pulse width of 1 s. Each data point represents the average of four samples. **d** The current change in response to light pulses (200 mW cm^{-2}) with various pulse widths. **e** The operating stability of the device during the application of 100 pulses (375 nm, 200 mW cm^{-2}) with 0.1 s width and 0.1 s pulse interval with a resting period of 150 s. **f** The chemical structure of four other n-type OMIECs. **g** The comparison of photocurrent generated by other n-type OECTs. The devices were illuminated by 375 nm light for 5 s at a light intensity of 200 mW cm^{-2}. The devices were operated in 0.1 M NaCl using Au gate electrode and had identical channel size.

writing capability (Fig. 2b and Fig. S11g). The device achieves these conductance states within a wide dynamic current range of 21.96 μA. Only after 340 s spent in the dark (ca. 3 times more time spent in recovery compared to stimulation) did the current return to its initial level, suggesting that the device shows somewhat charge storage ability induced by light (Fig. 2b).

Simultaneously, we explored the device response to varying wavelengths of light pulses applied at various durations and intensities. As the intensity of the pulsed light, as well as the duration it was on, increased, the current exhibited a corresponding increase, enabling continuous tuning of the device's conductance states (Figs. S12 and S13). Furthermore, our retina-inspired optoelectrochemical synaptic transistors demonstrated significant current modulation in response to light in the ultraviolet (UV), visible (VIS), and near-infrared (NIR) regions (Fig. S14). This multispectral sensitivity can be attributed to the broad absorption profile of p(C2F-z), enabling artificial multispectral visual perception. The synaptic weight of the device exhibited different behavior in response to varying light wavelengths, as depicted in Fig. S15. Unlike the absorption profile, the drain current (I_D) of the synaptic device decreased as the wavelength increased, attributed to the higher photo energy associated with shorter wavelengths[35]. Additionally, the photonic synaptic weight of the device could be controlled by adjusting the gate voltage, with higher biasing values leading to larger changes in I_D but a shorter recovery time (Fig. S16a, b and Supplementary Note 1).

In biological synapses, real-time recognition and decoding of visual information are closely associated with the phenomenon of paired-pulse facilitation (PPF) in the postsynaptic neuron. PPF represents a fundamental mechanism underlying diverse synaptic activities, where consecutive presynaptic stimuli result in the amplification of the postsynaptic signal. To determine if the device exhibits PPF behavior, we quantified the difference between the device's output when exposed to two sequential light pulses (375 nm, 200 mW cm^{-2}) with a t_p of 1 s, compared to a single pulse. As depicted in Fig. S16c, the second excitatory postsynaptic current (EPSC) (A_2) exhibited a higher amplitude than the first (A_1). The PPF index (A_2/A_1), a crucial parameter for evaluating the PPF ability, gradually decreased as Δt increased from 1 to 30 s (Fig. 2c). Increasing the pulse number or the training period improved the device's learning ability, suggesting spike-number and spike-time-dependent plasticity (Fig. S17a and Fig. 2d). These findings demonstrate the device's ability to transform plasticity from short-term (STP) to long-term (LTP) through repetitive rehearsal events occurring multiple times (Fig. S17b, c), over an extended period (Fig. 2d and Fig. S17d, e), and at varying frequencies (Fig. S17f). Notably, the device exhibited excellent stability, maintaining its current response even after undergoing 2000 s of operation (Fig. 2e).

Furthermore, we conducted a comparative analysis of the photocurrent generated by p(C2F-z) with those of commonly used OMIECs, including the commercially available BBL[36], the NDI-based p(C_6NDI-T)[25], and the BTI-based f-BTI2TEG-FT[37] and AIID-based gAIID-2FT[38] (Fig. 2f). The device characteristics are summarized in Table S3, and the optoelectrochemical characteristics are shown in Figs. S18–21. While all five materials exhibit a response to UV light, the high V_{TH} of especially for f-BTI2TEG-FT and gAIID-2FT devices leads to high operation voltage, (Figs. S20, 21 and Table S3) exceeding 1 V, which is unfavorable for subsequent operations. Moreover, only BBL and p(C_6NDI-T) devices are sensitive to the other wavelengths, that is, 455, 660 nm, and 1100 nm, although the response is relatively small. For all wavelengths of light, with identical device geometry and comparable operating conditions (at saturation and V_G that generates the highest photoresponse), p(C2F-z) has the highest photocurrents generated. For example, comparing the photoresponse of these materials with that of p(C2F-z) under UV light, we found that p(C2F-z) exhibited a response of 4.7 μA, while the other materials are at the nA level (Fig. 2g). The p(C2F-z) OECT showcased exceptionally high photoresponse at low operating voltages across the UV, VIS, and NIR spectral regions, highlighting its potential for visual bionics applications.

The synaptic function and its skin conformable form factor of p(C2F-z)

Incoming information is rapidly acquired and temporarily stored in the hippocampus as short-term memory. These memories can be consolidated into long-term memory through rehearsal learning. Our device exhibited a similar pattern: after the initial learning phase (100 excitation pulses) and subsequent forgetting, the current could be restored to its previous state using only 50 pulses (Fig. 3a). Continuous sequential learning can enhance the consolidation of long-term memories (Fig. S22a). Another way the human brain acquires information is through associative learning, where a connection is made between two stimuli or between a behavior and a consequence. Associative learning helps in forming long-term memories by creating strong connections between different pieces of information. We used long-term potentiation to simulate Pavlovian associative learning, as shown in Fig. 3b. Since this material has broad and distinct spectral sensitivity, we used two sets of consecutive spikes under different wavelengths of light (λ = 455 nm and λ = 375 nm) representing the "bell" and "beef" stimulus, respectively. A salivation response was defined as reaching a threshold of I_D = 17 μA. Prior to training, a sequence of 30 consecutive "bell" stimuli failed to elicit salivation, and salivation was triggered only after 30 consecutive "beef" stimuli. During the training phase, the device received "bell" and "beef" stimuli simultaneously, which resulted in observable salivation. After the training, a series of "bell" stimuli induced salivation, indicating the successful simulation of Pavlovian associative learning using p(C2F-z) based optoelectrochemical transistor in which the 455 nm light was associated with the beef.

Besides the ability of dynamic learning, a synaptic device could process information using logic functions. We leveraged our OMIEC's distinct current response to individual wavelengths of light and used two wavelengths as inputs to modulate the conductance of a single channel, generating OR and AND operations (Fig. 3c). When either Light 1 (375 nm) or Light 2 (455 nm) was turned ON, the excitatory postsynaptic current I_D surpassed the threshold (14.6 μA), indicating the "OR" logic operation (Fig. 3d, f). The I_D exceeded the threshold (14.6 μA) only when Light 1 and Light 2 were applied simultaneously, indicating the AND logical operation (Fig. 3e, f). Furthermore, the device effectively responded to both optical and electrical stimuli through the adjustment of the values of the bias and light intensity, demonstrating OR/AND gate operations regulated by a combination of the two input types (Fig. S22c–e). The I_D exceeded the threshold (16.8 μA) only when the high V_D and light were applied together, indicating the AND logic operation (Figs. S22c, e). When either voltage (high V_D or low V_D) or light was applied, the I_D surpassed the threshold (14 μA), generating the OR logical operation (Fig. S22d, e).

Considering the potential of this device to be integrated with living systems as the building blocks of an artificial retina or for light-based therapy, we evaluated the biocompatibility of p(C2F-z) through cell viability tests. Madin-Darby Canine Kidney (MDCK II) cells were cultured directly on top of the films, and as evidenced by live-dead cell staining assay, no significant differences in cell viability and adhesion were observed compared to the control group on glass (Fig. 3g and Fig. S23), suggesting that the material has negligible cytotoxicity and is biocompatible. The device is also compatible with fabrication in a flexible form that can then be attached to human skin through a hydrogel (Fig. 3h). The flexible OECT operated through the hydrogel exhibited stable optoelectrochemical characteristics (Fig. 3i and Fig. S24), similar to its performance in 0.1 M NaCl (Fig. S25).

https://doi.org/10.1038/s41467-025-56814-w

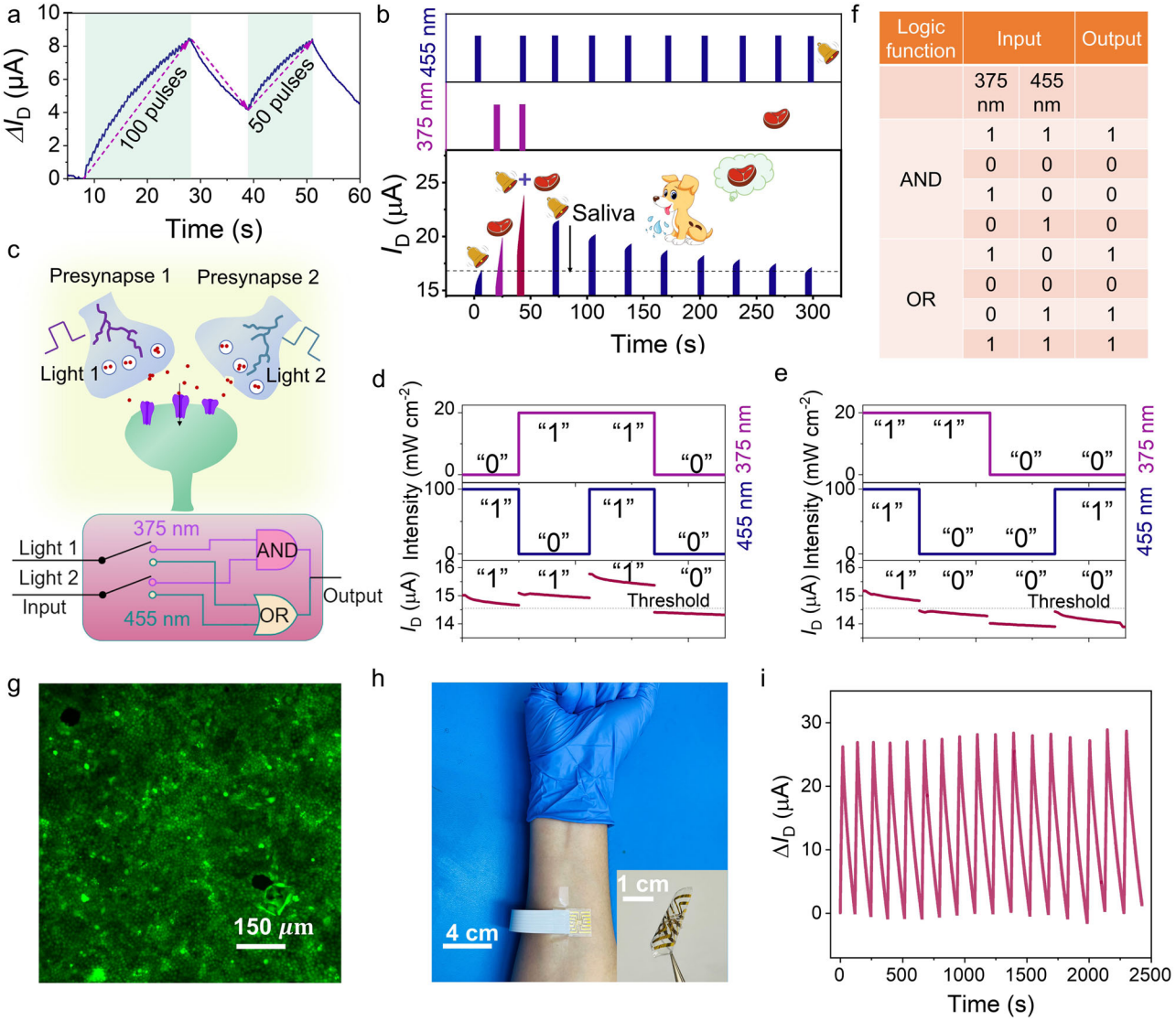

Logic function	Input		Output
	375 nm	455 nm	
AND	1	1	1
	0	0	0
	1	0	0
	0	1	0
OR	1	0	1
	0	0	0
	0	1	1
	1	1	1

Fig. 3 | The memory function of the optoelectrochemical synapse and its skin conformable form factor. a Learning behavior in which only a few pulses (50) restore the memory gained through training with more pulses (100). The light pulse was at 375 nm with 200 mW cm^{-2} intensity. **b** Complete associative learning process using two light sources with two wavelengths (λ=375 nm and λ=455 nm, 200 mW cm^{-2}). This process is similar to the conditioned and unconditioned stimuli in Pavlov's dog experiment. After the training (30 pulses of "bell", 30 pulses of "beef" and 30 pulses of "bell" and "beef"), the conditioned stimulus ("bell") can trigger unconditioned response (salivation). **c** The schematic diagram of optical logic functions of "AND" and "OR" operations of the optoelectrochemical synapse. The setup of optical logic functions of "AND" and "OR" operations is shown in Fig. S22b. The input (Light 1, 375 nm and Light 2, 455 nm) and output characteristics of the (**d**) "OR" operation and (**e**) "AND" operation. Light 1, "1": a low illumination intensity (20 mW cm^{-2}), and a high output current and "0": no light, a low output current; Light 2, "1": a high illumination intensity (100 mW cm^{-2}), and a high output current and "0": no light, a low output current. **f** The truth table of AND/OR logic functions. **g** Live/dead staining and cell viability. **h** The flexible and conformable optoelectrochemical synapse attached to skin. **i** The operating stability of the skin attached device. 100 pulses (375 nm, 200 mW cm^{-2}) with 0.1 s width and 0.1 s pulse interval were applied with a resting period of 98 s. The device was operated using commercial hydrogel as the electrolyte. $V_D = V_G = 0.4$ V.

The mechanism of light-induced electrochemical doping and memory generation

When light interacts with the conjugated backbone, excitons are formed. We hypothesize electrons that are dissociated from these excitons and introduced to the channel (photoinduced electron, Fig. 4a). These free charges perturb the open circuit potential (OCP) of the film and move it towards more negative values (Fig. S26a). To understand the impact of the OCP change on the device operation, we monitored the changes in the electrochemical potentials of the OECT terminals (gate, source, and drain) with respect to a reference electrode during electrochemical and photochemical doping (Fig. 4b). When a V_G and V_D of 0.4 V are applied, the potential of the source relative to the gate and the drain potentials decreases by 0.4 V, stabilizes at an electrochemical potential at approximately −0.12 V vs. Ag/AgCl reference electrode (Fig. 4c). The Au gate electrode has an electrochemical potential of 0.28 V vs. Ag/AgCl. As we turn on the LED, the electrochemical potentials of the gate, drain, and source electrode collectively drop to lower values. Upon light withdrawal, these potentials gradually increase to their pre-irradiation levels. Following a second cycle of illumination (Fig. S26b), the potential of the source drops again, with the magnitudes correlating with the light intensity.

The channel, getting more negatively polarized upon light exposure, should be attracting additional cations (right schematic of Fig. 4a). Operando eQCM-D measurements prove the increase in the number of electrolyte species accumulating inside the film during light exposure (Fig. 4d, Fig. S26c, d). The mass taken up by film (attributed

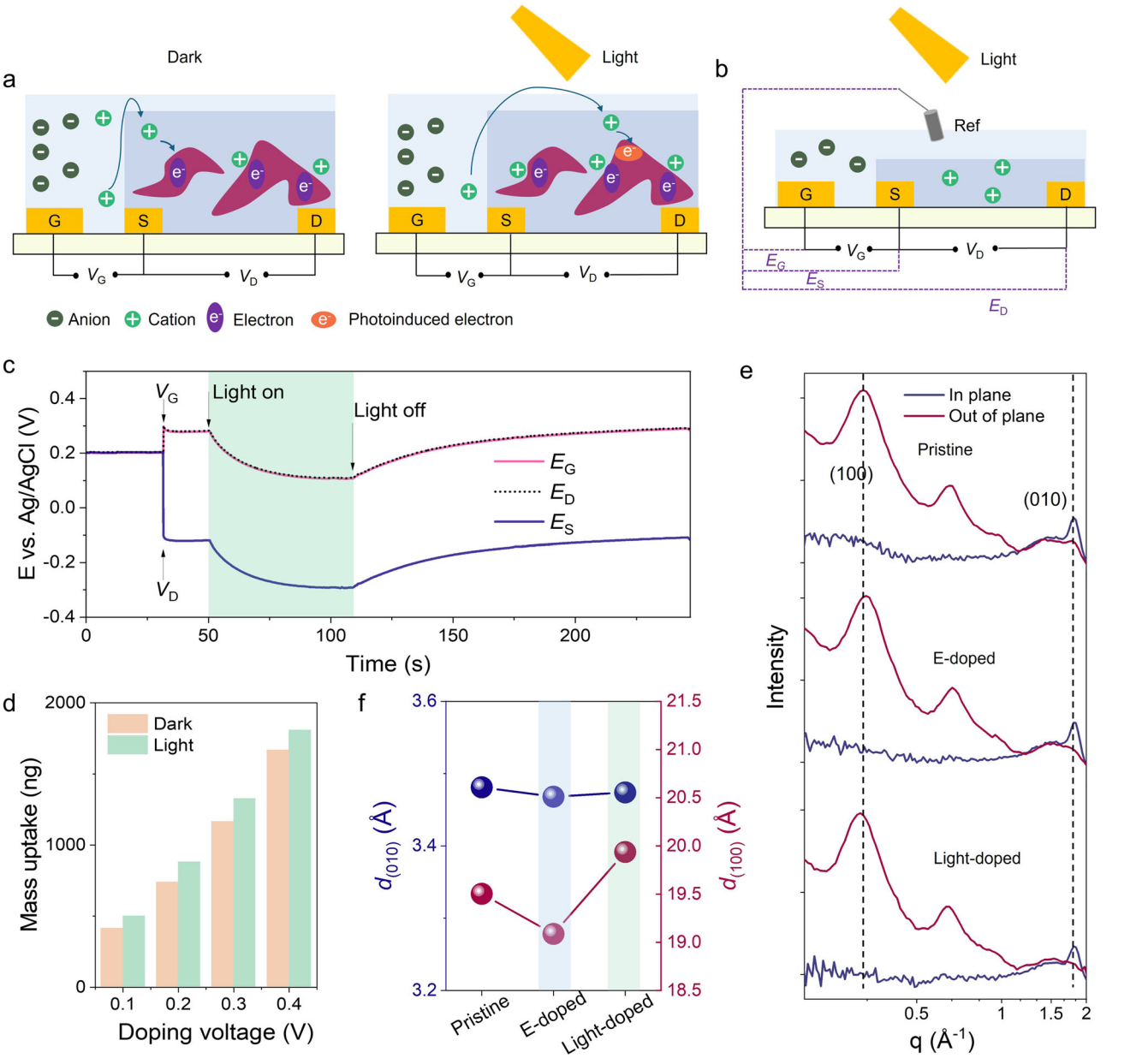

Fig. 4 | The operating mechanism of the optoelectrochemical synaptic device. The proposed mechanism of (**a**) charge carrier generation and ion transport while the channel is electrochemically doped (left), upon illumination (right). **b** The multichannel potentiostat setup to determine the electrochemical potential of transistor terminals with respect to the Ag/AgCl reference electrode during device operation (left). **c** The OCP change of the film during light exposure measured (right). E_G, E_D, E_S are electrochemical potentials of the device terminals during device operation relative to the gate, the drain and source potentials, respectively. V_D = 0.4 V and V_G = 0.4 V were applied at t = 30 s, the LED (200 mW cm^{-2}) was switched on at t = 50 s for 50 s, and the LED is switched off at 109 s. **d** The extent of mass uptake by the film during electrochemical doping and upon the addition of light illumination determined using eQCM-D performed using an optical module. **e** One-dimensional GIWAXS profile of the film in three different states: pristine (top), electrochemically-doped (middle), and doped by light (bottom, light intensity is 200 mW cm^{-2}). **f** The π-π stacking of (010) and lamella stacking of (100) distance.

to cations and water) during combined light and voltage biasing is higher than that during only electrochemical doping (Fig. 4d). The increase in the film mass and the current it generates (Fig. S27) during light exposure implies that the light irradiation drags more cations into the film, akin to the effect of applying higher voltage, which leads to an increase in its doping state. Upon light removal, the electrons may undergo recombination, and excess cations gradually leave the polymer, leading to a slow and nonlinear decay of channel current, which is reflected in the charge retention characteristics.

The light exposure seems to have a small effect on the microstructure, which we probed using ex-situ grazing-incidence wide-angle X-ray scattering (GIWAXS) (see Table S4 for peak parameters, Fig. S28 and Fig. 4e). During electrochemical doping, and photoelectrochemical doping, we observed minimal changes in the pi-pi stacking (010) of the film, with a distance of around 3.47 Å (Fig. 4f). However, a change in the lamellar stacking (100) was observed following both electrochemical doping and photoelectrochemical doping, as illustrated in Fig. 4f. After electrochemical doping, the lamellar stacking distance of the (100) decreases from 19.50 Å to 19.09 Å, which indicates slightly enhanced crystallinity (Fig. 4f and Table S4). However, upon photoelectrochemical doping, the lamellar stacking distance of the (100) increases from 19.09 Å to 19.94 Å, suggesting disrupted crystallinity. We speculate that this increase may be due to additional cation penetration during photoelectrochemical doping.

https://doi.org/10.1038/s41467-025-56814-w

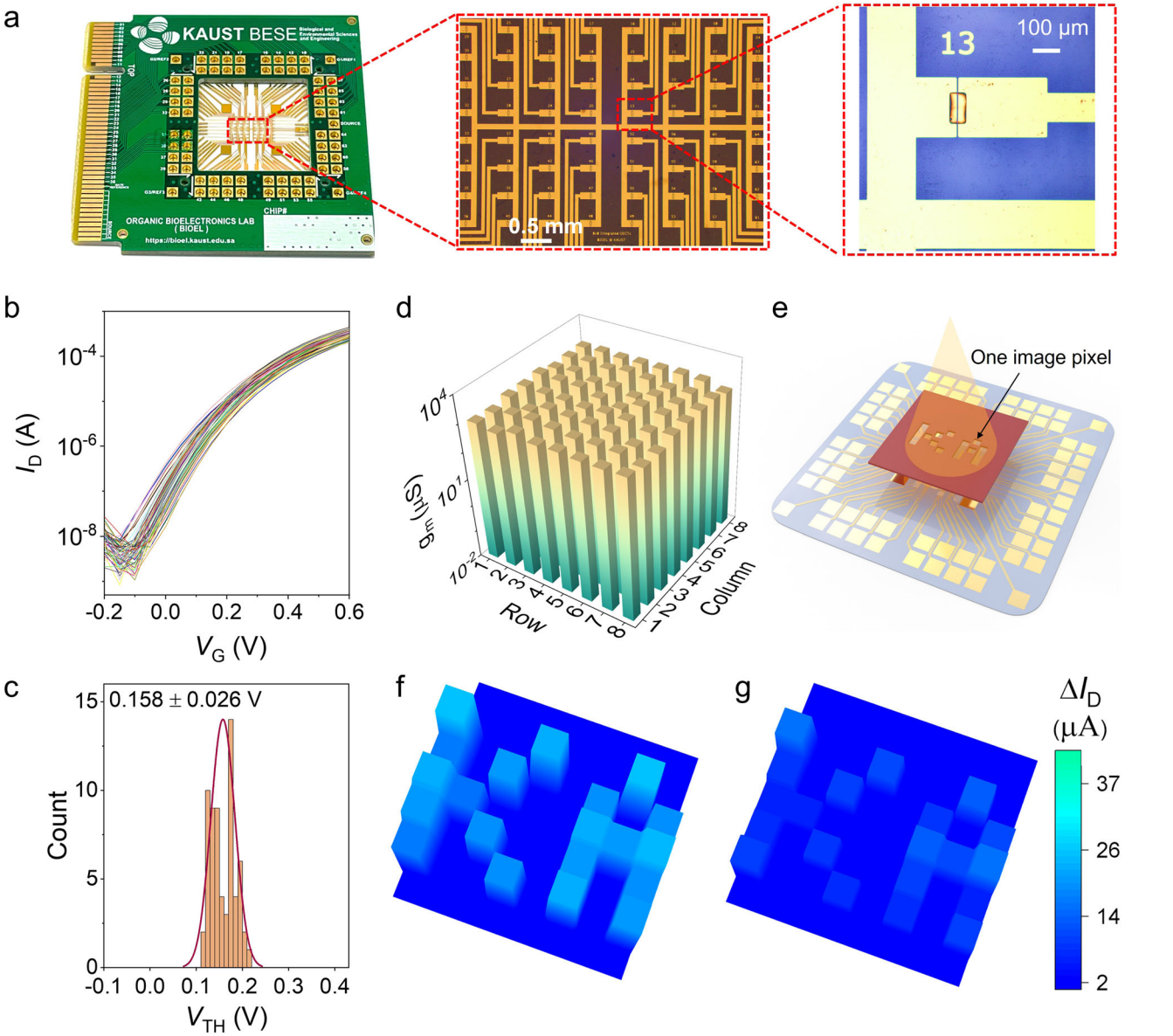

Fig. 5 | Synaptic array for image recognition and memorization. a The photograph of the synaptic array (left) with its magnified optical microscopy image (middle) and a single transistor channel (right). **b** Transfer characteristics of 64 p(C2F-z) OECTs (W/L = 100 μm/10 μm). **c** Transconductance distribution in the 8 × 8 synaptic array. **d** Statistical distribution histogram of the threshold voltage for 64 devices (all operational). **e** Schematic illustration of synaptic active-matrix arrays with a photomask patterning the letters 'KA'. Illustration of (**f**) the image adaptive perception and (**g**) the memorization of letters. The current change of the array was mapped (**f**) immediately and (**g**) 30 s after light (200 mW cm^{-2}) was switched off.

Synaptic array for image recognition and memorization

The p(C2F-z) OECT exhibits light intensity-dependent output currents and retention characteristics, resembling the human retina; hence, we hypothesized that it could enable image recognition and memorization. To evaluate this function, we fabricated 8 × 8 OECT arrays with dimensions of $W = 100$ μm and $L = 10$ μm (Fig. 5a). The OECT array was connected to a self-developed printed circuit board. We first recorded the transfer and transconductance characteristics of these 64 transistors throughout the entire area (Fig. S29a, see Supplementary Note 2 for experimental details) to assess the uniformity of channel response across the array. The transfer curves of the devices exhibited a concentrated distribution (Fig. 5b), demonstrating excellent uniformity with an average g_m of 1.39 ± 0.25 mS (Fig. 5c and Fig. S29b) and V_{TH} of 0.158 ± 0.026 V (Fig. 5d). The array was then illuminated through a photomask with a pattern displaying the letter 'KA', with each transistor channel corresponding to one image pixel (Fig. 5e). We measured the current change of 20 transistors immediately after light exposure (Fig. 5f) and 30-second post-light exposure (Fig. 5g). The current profile changed following the shape of these letters, showcasing image recognition capability of the device. Although weakly, the 'KA' shape can still be observed after the image was removed (Fig. S30).

Event-based in-sensor reservoir computing and full-color image processing

Reservoir computing is an emerging approach inspired by neuromorphic systems, particularly suited for efficient edge learning in dynamic signal processing. It maps temporal signals onto a high-dimensional feature space through a fixed dynamic system with fading memory, enabling effective analysis of time-dependent data. We leverage the spatiotemporal dynamics of our light responsive OECT, which exhibits nonlinear current responses to light stimuli, to design a reservoir encoder that effectively preprocesses and extracts information

https://doi.org/10.1038/s41467-025-56814-w

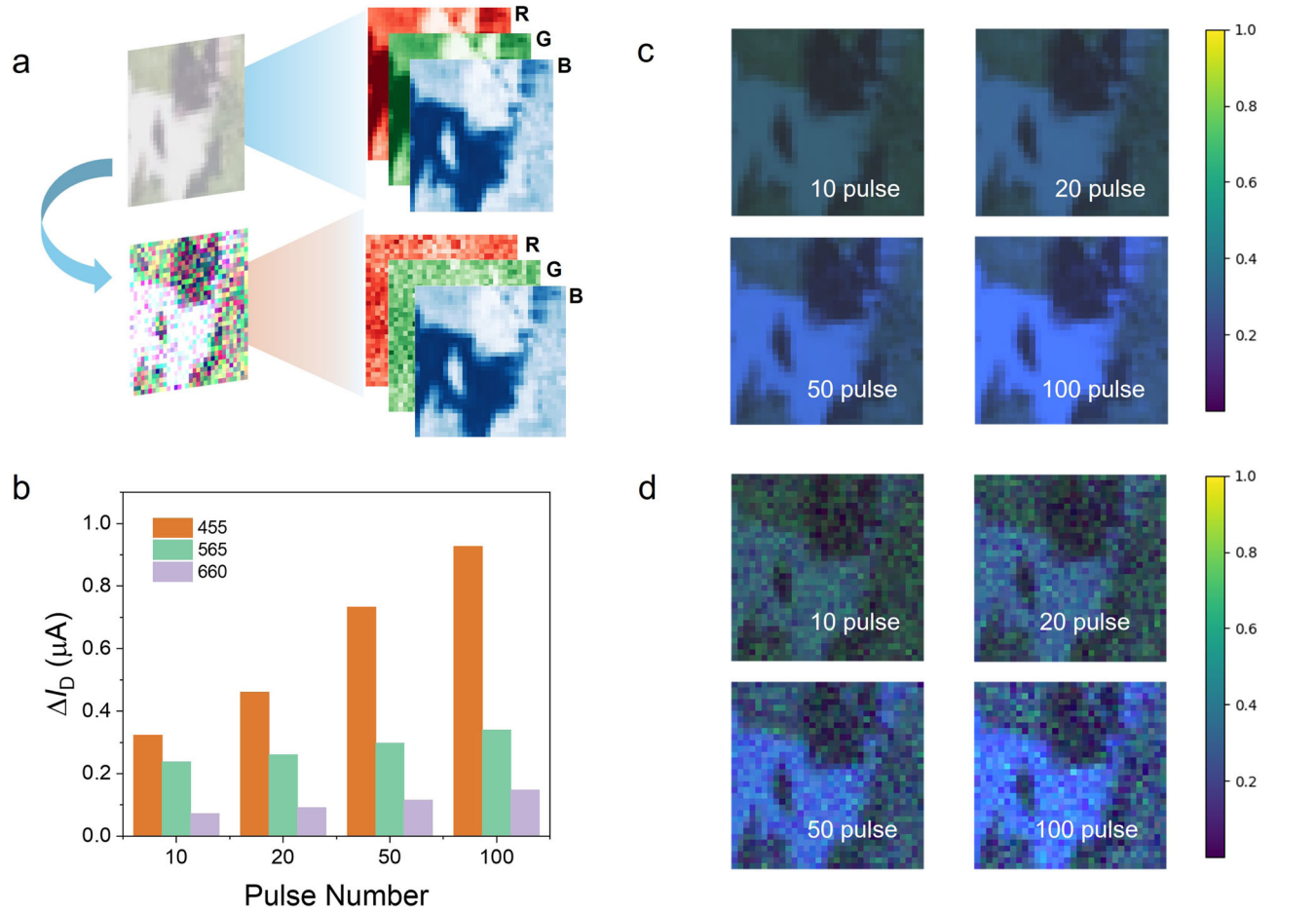

Fig. 6 | Full-color image processing. a A schematic for the color information encoding process. **b** The channel current change as a function of pulse number under different light sources: red (660 nm), green (565 nm), and blue (455 nm). The contrast between the blue and other features increases in the (**c**) original image and (**d**) noisy image with the number of light pulses.

from event-based data. To evaluate the performance of our OECT as a reservoir encoder, we first recorded the current evolution in response to sixteen 4-bit optical pulses, each lasting for 1 s, with a time interval of 1 s. The presence of light with an intensity of 200 mW cm^{-2} was represented by '1', and its absence by '0'. A '1' input resulted in an increase in ΔI_D, while a '0' led to a decrease, creating 16 distinct states ranging from (0000) to (1111), as shown in Fig. S31a. These optical stimuli, representing different states, were then directly input into the reservoir computing system using the neuromorphic MNIST dataset (NMNIST). The schematic of our proposed approach is illustrated in Fig. S31b. Each NMNIST sample comprises spike-based data with ON and OFF events, represented by changes in the optical signal. Our array, with its short-term dynamic response, can process these optical streams, serving as both an image sensor and a reservoir encoder. The extracted data is subsequently fed into a spike neural network (SNN) for further classification, as illustrated in Fig. S31c. The circuit diagram of the reservoir is shown schematically in Fig. S31d. Synaptic transistors receive varying light stimuli, generating corresponding channel currents (Fig. S31a), which are then converted into voltages by trans-impedance amplifiers and digitized through analog-to-digital converters (ADCs) for further processing (Fig. S31d). The confusion matrix post-training is displayed in Fig. S31e. Overall, our reservoir-computing system, based on a water-compatible organic transistor array, achieved an accuracy of 95.71%, comparable to that of the single-layer SNN (98.63%) and the double-layer SNN (98.78%) (Fig. S31f, Fig. S32 and Supplementary Note 3).

Leveraging the device's sensitivity to specific wavelengths, we next explored its differential response to R, G, and B light for full-color image pre-processing. A sample color image from the CIFAR-10 dataset was decomposed into R, G, and B channels, with Gaussian random noise added to the R and G channels to simulate noisy conditions (Fig. 6a). During the mapping process, the R, G, and B pixel values were assigned to corresponding light pulse intensities at their respective wavelengths. The device's noise reduction capability was influenced by its wavelength-specific photoresponsivity, with a notably higher photocurrent response to blue light (455 nm) compared to longer wavelengths. We evaluated the photoresponsivity using varying pulse counts (10, 20, 50, and 100), as shown in Fig. 6b. With increasing pulse numbers, the contrast between blue features and other components of the image was enhanced, significantly improving the clarity of both the original and noisy images (Fig. 6c, d). This result demonstrates that repeated light pulses selectively emphasize blue features within the image, effectively isolating them due to the device's wavelength-specific sensing properties. The methodology for this color image preprocessing approach is described in further detail in Supplementary Note 4.

The voltage-controlled synaptic device operation for motion perception

One important feature of the p(C2F-z) OECT based optical synapse is its ability to respond to electrical cues, mimicking the behavior of biological neurons. When stimulated the synapse with an electrical pulse at a frequency of 100 Hz, the channel current exhibited a gradual increase until saturation (Fig. 7a), resembling the response of graded neurons. Graded neurons efficiently encode temporal information

https://doi.org/10.1038/s41467-025-56814-w

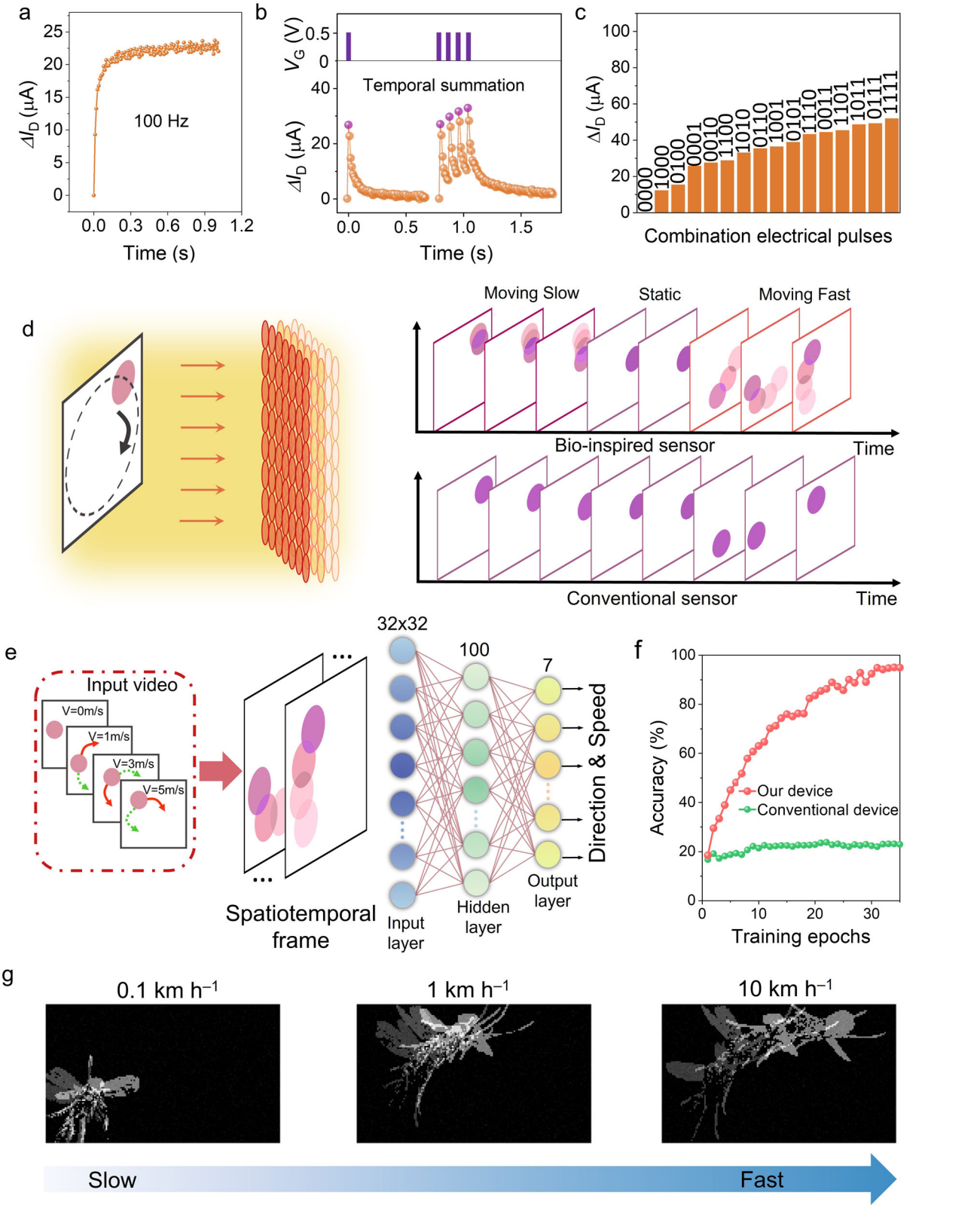

Fig. 7 | Motion detection with organic optoelectrochemical synapse. Change in I_D as a function of time upon (**a**) a single electrical pulse at a frequency of 100 Hz, (**b**) a single electrical pulse (V_G = 0.5 V, pulse width = 5 ms) and four consecutive pulses (V_G = 0.5 V, 5 ms on and 80 ms off). V_D = 0.5 V. **c** Response to four-bit electrical stimulation. '1' and '0' represent the stimulation at V_G = 0.5 V and V_G = 0 V, respectively. **d** The sample motion video captured by a sensor array. The bioinspired sensor can extract temporal and spatial information, while the conventional image sensor only generates spatial information because it captures images at fixed time intervals. **e** A small network is used to classify the extracted feature and identify the moving speed and direction. **f** The recognition accuracy comparison with our device and a conventional sensor. **g** The OECT sensor generates different spatiotemporal frames depending on the speed of motion.

from photoreceptor inputs by exhibiting temporal summation without a refractory period, allowing for the encoding of spatiotemporal information related to moving objects (see Fig. S33 and Supplementary Note 5 for details)[39,40]. By applying a sequential electrical stimulus pattern, we observed that the synapse emulated this behavior, demonstrating temporal summation characteristics (Fig. 7b).

In addition to the number of gate pulses, the magnitude of the gate voltage significantly influenced the synaptic weight of the device. Higher gate voltages resulted in a more pronounced change in the channel current (Fig. S34a). The device's electrical response was further tested using sequences of electrical pulses, where '1' and '0' represented $V_G = 0.5$ V and $V_G = 0$ V conditions, respectively. Figure 7c illustrates the change in I_D under 16 distinct stimulation patterns of four pulses, each lasting 5 ms with a 5 ms interval. I_D depended precisely on the sequence of electrical stimulation. Finally, to evaluate long-term stability, the synapse was subjected to 185 unique stimulation patterns, with each pattern comprising four consecutive electrical pulses and a resting period of 0.95 s between sequences (Fig. S34b). The device exhibited excellent stability and reliability throughout these extended tests, further supporting its potential for encoding temporal information in neuromorphic applications.

To demonstrate the capability of the device to integrate spatial and temporal dynamics, it was applied to high-accuracy motion recognition in machine vision applications. To evaluate its motion perception abilities, we used the device to classify the direction and speed of moving balls (Fig. 7d, see Fig. S35 and Supplementary Note 6 for details). By extracting a feature map from event-based data, the sensor array provided input to a compact artificial neural network (ANN) for motion detection (Fig. 7e). The sensor's ability to capture both spatial and temporal dynamics enabled the creation of a spatiotemporal feature map, which provided comprehensive information about movement behavior, including direction and velocity, critical for accurate classification. In contrast, conventional sensors acquire spatial information from individual frames but do not encode temporal dynamics within the data (see Supplementary Note 6 for details). Figure 7f compares the recognition accuracy during the training process between our device and a conventional image sensor. The bio-inspired sensor achieved a recognition accuracy of 92.5% after 30 training epochs, surpassing the performance of the conventional image sensor (approximately 22.4%). Furthermore, the neural network exhibited robustness to device-to-device variations, maintaining a training recognition accuracy above 80% even with a 30% variation in device conductance (Fig. S36), demonstrating the network's tolerance to non-ideal conditions.

The device was further evaluated in real-world scenarios (Fig. 7g), showcasing its ability to decode spatiotemporal information across various timescales. For instance, it successfully captured and compressed 3D motion data into 2D frames that preserved information about speed and direction. This capability was demonstrated by detecting and classifying the motion of moving balls in terms of both velocity and direction. These results suggest that the system can capture diverse sensory actions, mimicking the functionality of retinal neurons.

Discussion

This work presents a biomimetic optoelectrochemical synapse based on a single-component, photoactive, and biocompatible n-type organic mixed conductor, demonstrating significant potential for neuromorphic systems and prosthetics. The semiconductor features a fluorinated bisisatin-lactone-bithiazole backbone functionalized with polar oligoethylene glycol side chains, enabling the uptake and transport of ionic charges within microscale films. Implemented as an aqueous electrolyte-gated transistor, the device leverages its mixed conductor design to achieve linear, multilevel conductance states of 9 bits. Our synapse uniquely perceives multispectral visual information spanning ultraviolet, visible, and near-infrared wavelengths, exhibiting a high photoresponse in aqueous media that distinguishes it from other OMIECs used in miniaturized OECTs. The device's ability to scale current changes with the number of light pulses emulates key biological synaptic behaviors, including synaptic plasticity, pair-pulse facilitation, and light-triggered logical functions as well as Pavlovian conditioned reflexes. This functionality originates from the light-induced ion uptake and subsequent electrochemical doping of the film bulk, with memory effects attributed to the slower recombination of separated charges interacting with electrolyte ions.

We designed an integrated synaptic array based on this transistor with remarkable channel performance uniformity and used it for adaptive image recognition and memory storage. The combination of optical response and its dynamics enables efficient encoding and processing of optical data streams, facilitating an event-based in-sensor reservoir computing framework. Additionally, the p(C2F-z) OECT is programmable via electrical stimuli, allowing for the integration of electrical training signals to extract spatiotemporal information, enabling motion perception. Finally, the film's biocompatibility and processability into flexible devices open pathways for the development of advanced prosthetics with integrated sensing, processing, and storage capabilities. Overall, this work introduces a water-compatible organic photoactive n-type mixed conductor as an optoelectrochemical synapse, offering a versatile platform for applications in neuromorphic systems, adaptive electronics, and prosthetics.

Methods

Materials

Reagents for synthesis were purchased from commercial suppliers unless otherwise indicated. Solvents for spectroscopic studies were of spectroscopic grade, purchased from Sigma-Aldrich, and used as received. Synthetic intermediates and final monomers were purified using column chromatography with silica gel (General-Reagent, 200-300 mesh) using dichloromethane, ethyl acetate, and methanol. Polymers were purified using sequential Soxhlet extractions in various solvents. ^{1}H and ^{13}C NMR spectra were recorded in $CDCl_3$ or 1,1,2,2-tetrachloroethane-d2 (TCE-d2) with a 400 or 500 MHz Bruker Avance III spectrometer.

Cyclic voltammetry (CV) and electrochemical impedance spectroscopy (EIS)

For CV measurements in the organic electrolyte, an Ag/AgCl was used as the reference electrode, a Pt wire as the counter electrode, and the ferrocene/ferrocenium couple (Fc/Fc^+) was used as an external standard to calculate LUMO. Aqueous CV measurements were conducted in 0.1 M NaCl at the scan speed of 0.1 V/s. Using standard photolithography procedures, we fabricated the multi-electrode arrays similarly to OECTs (see below). Several electrode geometries with various areas ranging from 0.0016 cm^2 to 0.0064 cm^2 were patterned on glass substrates and insulated with parylene C. Impedance spectra were acquired using a standard 3-electrode set-up, with the WE being the polymer-coated gold electrodes, the CE being a Pt wire, and the RE being an Ag/AgCl electrode, all immersed in NaCl 0.1 M. The working electrode's potential was changed in −0.1 V steps, with an AC modulation of 10 mV. Capacitance (C) was calculated using the reactance of the imaginary component of the impedance according to the equation:

$$C = \frac{1}{2\pi f |Z''|} \quad (1)$$

To calculate the C*, the calculated capacitance was normalized to the volume of the electrodes. The thickness, determined using an atomic force microscope, was 79 ± 15 nm for p(C2F-z).

Light source

We used a DC2200 LED Driver (ThorLabs) operating ThorLabs mounted LEDs for the light irradiation. The different ThorLab light sources we used are as follows: UV LED (M375L4), Royal Blue LED (M455L4), Deep Red LED (M660L4) and Infra-Red LED (M1100L4). The light source calibration and conversion from LED current input (from the driver controller) to light intensity output was performed with the digital optical power and energy meter (PM100D, ThorLabs) combined with the slim photodiode power sensor (S130VC, ThorLabs). The distance between the OMIEC (or photodiode during calibration) and the light source was maintained at 1 cm throughout the study.

Cell culture

Madin-Darby Canine Kidney cells (MDCK II) were maintained in high glucose DMEM media supplemented with 5% fetal bovine serum, 2 mM Glutamax, and 0.5% PenStrep 100X (10000 U/mL Penicillin, 10 000 µg/mL Streptomycin) at 37 °C and 5% CO_2 in a humidified incubator. Round glass (25 mm) coverslips were spun coated with p(C2F-z) polymer at 500 rpm s^{-1} for 45 s. They were placed on a 6-well plate and MDCK II cells (P.32) were seeded at a density of 6000 cells/cm^2. After 24 h of culture, cell viability was assessed using a live and dead assay. Cells were incubated with 2 µm Hoechst, 3µm Calcein AM, and 3.5 µm Propidium Iodide (PI) in PBS containing Ca^{2+} and Mg^{2+}, for 15 min at 37 °C. Fluorescence images were captured using a 10X objective in an inverted Leica DMi8 microscope. A green signal is emitted by live cells as Calcein AM interacts with viable cells; on the contrary, PI reacts with the nuclei content of dead cells, generating a red signal, and Hoechst emits blue fluorescence when it binds dsDNA in the cell nuclei.

Device fabrication and characterization

The single-channel OECT and the OECT arrays were microfabricated on the 4-inch glass wafers with the same protocols using standard photolithography and parylene C (PaC) peel-off techniques. a first layer of photoresist (AZ5214) was spin-coated and exposed to ultraviolet light using a contact aligner. The photoresist patterns were generated with an AZ726 developer, followed by metal sputtering of 10 nm Cr and 100 nm Au and a standard lift-off process using hot dimethyl sulfoxide to create electrodes and interconnection pads. After that, 2.7 g of dichloro-[2,2]-paracyclophane (Diener Electronic) was deposited as a PaC insulation layer on the Au interconnects. Another 3.5 g of dichloro-[2,2]-paracyclophane was deposited as the second layer of PaC after spin-coating an anti-adhesive layer (3 vol % Micro-90 water solution, 1000 rpm. for 30 s) on the wafer. Then, a second layer of photoresist (AZ10XT) was spin-coated and exposed to ultraviolet light using a contact aligner. After developing the photoresist using AZ726 developer and reactive ion etching the surface, the patterns of contact pads were exposed. The p(C2F-z) film was spin-coated (500 rpm, 45 s) from a hexafluoroisopropanol solution (5 g L^{-1}) on the substrates to yield a film thickness of ca. 79 ± 15 nm in the channel. Finally, the second layer of PaC was peeled off to pattern the OECT channel. All devices were rinsed with deionized water before use. The devices were annealed at 150 °C for 20 min. The flexible OECT was microfabricated using the same protocol above but on a PaC substrate. 15 g of dichloro-[2,2]-paracyclophane was deposited as the PaC substrate on the 4-inch glass wafer after spin-coating an anti-adhesive layer at the beginning. The subsequent steps were the same with glass-substrate OECT. The PaC substrate, together with the insulation layer, yields a thickness of ca. 13 µm. A 0.1 M NaCl aqueous solution was used as the electrolyte, with a silver pellet serving as the gate. A PDMS well was utilized as a reservoir to contain the aqueous electrolyte. OECT device characterization, including transfer and output characteristics, along with repetitive pulsing measurements, was performed in air at room temperature using a dual source-meter unit (Keithley 2636 A) with a scan rate of 250 mV/s. The maximum geometry-normalized transconductance is calculated according to $g_{m,norm} = g_m W^{-1} L d^{-1}$. The threshold voltage (V_{TH}) was determined by extrapolating the linear regime of the $I_D^{1/2} \sim V_G$ plot. The product μC^* was extracted from the slope of the linear fit to g_m vs. $(W/L)(V_{TH} - V_G)$ plot, where C^* was extracted from electrochemical impedance spectra, and mobility (μ) was calculated using μC^* divided by C^* value. All OECTs were operated in a 0.1 M NaCl aqueous solution under ambient conditions. Average values were calculated from 5 operational channels.

The 'KA' shadow mask was laser-cut from the Dupont KAPTON® polyimide film (125 µm) by the laser cutter (VLS 3.50 10.6 µm Laser Platform), with a window size of 1 × 1 mm^2 per exposed channel. Device characterization was performed in air at room temperature using a dual source-meter unit (Keithley 2636 A) and an electrical probe station with a scan rate of 250 mV/s.

X-ray photoelectron spectroscopy (XPS)

XPS analysis was carried out using a Kratos Axis Supra instrument equipped with a monochromatic Al Kα X-ray source (hν = 1486.6 eV), which was operated at a power of 150 W and under ultrahigh vacuum (in the range of 10^{-9} mbar). All spectra were recorded in the hybrid mode using electrostatic and magnetic lenses. The obtained spectra were calibrated using the reference C 1 s at 284.8 eV.

Scanning transmission electron microscopy (STEM) measurements

The cross-section of the samples was prepared with a focused ion beam (FIB). TEM lamellas were prepared with a Helios G4 FIB-SEM dual-beam system (Thermo Fisher Scientific) equipped with a Ga+ ion source. A protective Pt layer was sputter-coated on the sample surface using a Luxor^{Pt} sputter-coater and additional Pt layer was deposited by FIB on the region of interest to further protect the polymer layer during the Ga ion milling for lamella preparation. Samples were thinned down to a relative thickness of 80 nm using progressively decreasing ion beam energies in the FIB down to 5 keV. Scanning transmission electron microscopy (STEM) images were taken with a FEI Themis-Z transmission electron microscope operated at 300 kV.

Operando electrochemical quartz crystal microbalance with dissipation monitoring (eQCM-D)

Measurements were performed using the QSense Analyzer, a QSense Window Electrochemistry Module (QWEM 401) from Biolin Scientific, and gold with titanium adhesion layer sensors (QCM5140TiAu120-050-Q) from Quartz Pro. The analyzer measured the shift and dissipation of the 1st, 3rd, 5th, 7th, 9th, and 11th frequency harmonics, which provide information about the changes in sample mass and softness. First, the bare sensors were measured in air and after NaCl (aqueous) 0.1 M was introduced into the module chamber. The electrolyte resulted in a large shift in the QCM-D signals due to the change in media density inside the chamber, which was adjusted for when calculating polymer swelling. After acquiring the bare sensor QCM-D baseline signals in both dry and wet conditions, the sensor was coated with a polymer film and placed back into the analyzer. The QCM-D signals were recorded again in dry state and with electrolyte after making sure that the frequency, f, and dissipation, D, signals were stabilized (i.e., Δf <1 Hz per 1 h), typically taking up to several hours, depending on the extent of passive swelling. Using the QSoft software function "stitch data" provided the difference between the f and D signals before and after the sensor was coated with a polymer film in both dry state and with electrolyte. This difference was used to calculate the film areal mass in dry and swollen states, using the Sauerbrey equation:

$$\frac{\Delta m}{A} = -\Delta f_n \frac{\rho_q V_q}{2 f_0^2 n} \approx \frac{-\Delta f_n}{n} 17.9 ng\, cm^{-2} \quad (2)$$

where Δf_n is the frequency shift of the nth overtone, A is the sensor active area, ρ_q is the density of quartz, V_q is the shear wave velocity in

quartz, f_0 is the fundamental frequency and n is the overtone number. Film thickness was calculated by dividing the calculated areal mass with film density. In the case where the films no longer retain their rigid characteristics, an increase in quartz oscillation energy loss—dissipation is observed. Increased dissipation indicates that the films have become soft and can no longer be approximated using the Sauerbrey method. The films are then approximated to behave as Kelvin-Voigt elements, meaning they exhibit viscoelastic properties, and can be described by the equation:

$$G^* = \mu + 2\pi i f \eta \tag{3}$$

where G* is the complex shear modulus, μ is elasticity (kg m^{-1} s^{-2}), η is viscosity (kg m^{-1} s^{-1}) and f is the frequency. To calculate the mass changes of a thick, viscoelastic film, complex shear modulus was analyzed and fitted using multiple overtones (chosen according to best quality fits). Q-Tools software was used for the modeling and data analysis. Swelling in Fig. S8e was calculated as the percentage change in volume relative to the dry volume:

$$swelling_{total} = \frac{Vol_{total} - Vol_{dry}}{Vol_{dry}} \times 100\,\% \tag{4}$$

eQCM-D and light-induced eQCM-D were performed using an Autolab PGstat128N potentiostat coupled with a QSense window electrochemistry module (QWEM 401). The integrated three-electrode setup comprised an Ag/AgCl reference electrode, Pt counter electrode, and the polymer-coated Au QSensor acting as the working electrode with an electrochemical active area of 0.7854 cm^2. The LED was positioned on the top QSense window module, with its intensity calibrated to 200 mW/cm^2, consistent with the light experiments. Before applying a potential to the film for light-induced eQCM-D measurements, a baseline was recorded to calibrate frequency and dissipation changes corresponding to mass uptake during electrochemical doping. The current was recorded using an Autolab PGstat128N potentiostat during doping at various potentials in dark and illuminated conditions.

UV-VIR-NIR absorption spectroscopy

Active layers were spun on clean glass substrates for steady-state absorption measurements. Measurements were performed using an Ocean Optics HL-2000-FHSA halogen light source, directed through a redox.me sample holder (MM SPECTRO-EFC) using QP600-1-SR-BX optical fibers and fed back to the Ocean Optics QE65 Pro Spectrometer. The OceanView software was first calibrated using a blank ITO substrate placed in the sample holder. The polymer films were spin-coated on ITO substrates and placed into the sample holder in direct contact with 1.3 mL of 0.1 M NaCl (aq). Potential steps of 0.1 V were applied to dope the films. Absorbance was recorded using OceanView software after 10 s of voltage application as the spectra stabilized.

Grazing-incidence wide-angle X-ray scattering (GIWAXS)

Samples for X-ray scattering were prepared using the same procedures for casting the polymeric channel in device fabrication except using pure silicon wafers as the substrate. An incidence angle of 0.18° and a photon energy of 8 keV were used to record the scattering patterns.

Graded neuron for motion perception

We demonstrated motion recognition of the solid ball with a customized video dataset based on OpenCV. We conducted vison-system simulations based on both bio-inspired vision sensors and conventional image sensors with the same network architecture. It included a 32 × 32 sensor array and a 3-layer perceptron with a 784 × 100 × 7 structure. The classic backpropagation algorithm was utilized for system training and testing. Each video frame was configured with dimensions of 32 × 32 pixels and the ball's velocity was set as 0, 1, 3, and 5 m/s, respectively, each in two different directions. The spatial information in the video highlights the relative pixel positions, and the temporal information tracks pixel changes over time. We extracted both spatial and temporal information with our sensor array, thus achieving the recognition of ball motion.

Data availability

The data that support the findings of this study are available within the article, its Supplementary Information, or from the authors.

References

1. Kim, Y. et al. A bioinspired flexible organicartificial afferent nerve. *Science* **360**, 998–1003 (2018).
2. Jung, Y. H., Park, B., Kim, J. U. & Kim, T. I. Bioinspired electronics for artificial sensory systems. *Adv. Mater.* **31**, e1803637 (2019).
3. Dai, S. et al. Emerging iontronic neural devices for neuromorphic sensory computing. *Adv. Mater.* **35**, e2300329 (2023).
4. Choi, C., Lee, G. J., Chang, S., Song, Y. M. & Kim, D. H. Nanomaterial-based artificial vision systems: From bioinspired electronic eyes to in-sensor processing devices. *ACS Nano* **18**, 1241–1256 (2024).
5. Shao, H. et al. A reconfigurable optoelectronic synaptic transistor with stable Zr-CsPbI(3) nanocrystals for visuomorphic computing. *Adv. Mater.* **35**, 2208497 (2023).
6. Seo, S. et al. An optogenetics-inspired flexible van der waals optoelectronic synapse and its application to a convolutional neural network. *Adv. Mater.* **33**, 2102980 (2021).
7. Wang, Y. et al. Optoelectronic synaptic devices for neuromorphic computing. *Adv. Intell. Syst.* **3**, 2000099 (2020).
8. Zhou, F. et al. Optoelectronic resistive random access memory for neuromorphic vision sensors. *Nat. Nanotechnol.* **14**, 776–782 (2019).
9. Zhang, Y., Huang, Z. & Jiang, J. Emerging photoelectric devices for neuromorphic vision applications: principles, developments, and outlooks. *Sci. Technol. Adv. Mater.* **24**, 2186689 (2023).
10. Chen, K. et al. Organic optoelectronic synapse based on photon-modulated electrochemical doping. *Nat. Photonics* **17**, 629–637 (2023).
11. Harikesh, P. C. et al. Ion-tunable antiambipolarity in mixed ion-electron conducting polymers enables biorealistic organic electrochemical neurons. *Nat. Mater.* **22**, 242–248 (2023).
12. Sarkar, T. et al. An organic artificial spiking neuron for in situ neuromorphic sensing and biointerfacing. *Nat. Electron.* **5**, 774–783 (2022).
13. Zhao, Y. et al. Side chain engineering enhances the high-temperature resilience and ambient stability of organic synaptic transistors for neuromorphic applications. *Nano Energy* **104**, 107985–107995 (2022).
14. Xie, Z. et al. All-solid-state vertical three-terminal n-type organic synaptic devices for neuromorphic computing. *Adv. Funct. Mater.* **32**, 2107314 (2022).
15. Wang, S. et al. An organic electrochemical transistor for multi-modal sensing, memory and processing. *Nat. Electron.* **6**, 281–291 (2023).
16. Zhao, Y. et al. Donor engineering tuning the analog switching range and operational stability of organic synaptic transistors for neuromorphic systems. *Adv. Funct. Mater.* **32**, 2205744 (2022).
17. Wang, Y. et al. Designing organic mixed conductors for electrochemical transistor applications. *Nat. Rev. Mater.* **9**, 249–265 (2024).
18. Guo, K. et al. Rapid single-molecule detection of COVID-19 and MERS antigens via nanobody-functionalized organic electrochemical transistors. *Nat. Biomed. Eng.* **5**, 666–677 (2021).
19. Rivnay, J. et al. Organic electrochemical transistors with maximum transconductance at zero gate bias. *Adv. Mater.* **25**, 7010–7014 (2013).
20. Li, P. et al. N-type semiconducting hydrogel. *Science* **384**, 30 (2024).

21. Huang, W. et al. Vertical organic electrochemical transistors for complementary circuits. *Nature* **613**, 496–502 (2023).
22. Gkoupidenis, P. et al. Organic mixed conductors for bioinspired electronics. *Nat. Rev. Mater.* **9**, 134 (2024).
23. Wang, H. et al. A ferroelectric/electrochemical modulated organic synapse for ultraflexible, artificial visual-perception system. *Adv. Mater.* **30**, e1803961 (2018).
24. Almulla, L. et al. N-Type polymeric mixed conductors for all-in-one aqueous electrolyte gated photoelectrochemical transistors. *Mater. Horiz.* **11**, 2937–2949 (2024).
25. Druet, V. et al. A single n-type semiconducting polymer-based photo-electrochemical transistor. *Nat. Commun.* **14**, 5481 (2023).
26. Hu, J. et al. A photoelectrochemical retinomorphic synapse. *Adv. Mater. 36*, 2405887–2405896 (2024).
27. Corrado, F. et al. Azobenzene-based optoelectronic transistors for neurohybrid building blocks. *Nat. Commun.* **14**, 6760 (2023).
28. Zhang, J. et al. Retina-inspired artificial synapses with ultraviolet to near-infrared broadband responses for energy-efficient neuromorphic visual systems. *Adv. Funct. Mater.* **33**, 2302885–2302897 (2023).
29. Chen, H., Cai, Y., Han, Y. & Huang, H. Towards artificial visual sensory system: Organic optoelectronic synaptic materials and devices. *Angew. Chem. Int. Ed. Engl.* **63**, e202313634 (2024).
30. Gong, X. et al. High-detectivity polymerphotodetectors with spectral responsefrom 300 nm to 1450 nm. *Science* **325**, 1665 (2009).
31. Yu, R. et al. Low-voltage solution-processed artificial optoelectronic hybrid-integrated neuron based on 2D MXene for multi-task spiking neural network. *Nano Energy* **99**, 107418–107426 (2022).
32. Wang, Y. et al. Acceptor functionalization via green chemistry enableshigh-performance n-type organic electrochemicaltransistors for biosensing, memory applications. *Adv. Funct. Mater.* **34**, 2304103 (2023).
33. Wang, Y. et al. Green synthesis of lactone-based conjugated polymers for n-type organic electrochemical transistors. *Adv. Funct. Mater.* **32**, 2111439 (2022).
34. Zeglio, E. et al. Mixing insulating commodity polymers with semiconducting n-type polymers enables high-performance electrochemical transistors. *Adv. Mater.* **36**, 2302624 (2024).
35. Park, H. L. et al. Retina-inspired carbon nitride-based photonic synapses for selective detection of UV light. *Adv. Mater.* **32**, 1906899 (2020).
36. Sun, H. et al. Complementary logic circuits based on high-performance n-type organic electrochemical transistors. *Adv. Mater.* **30**, 1704916 (2018).
37. Feng, K. et al. Fused bithiophene imide dimer-based n-type polymers for high-performance organic electrochemical transistors. *Angew. Chem. Int Ed. Engl.* **60**, 24198–24205 (2021).
38. Wang, Y. et al. n-type organic electrochemical transistors with high transconductance and stability. *Chem. Mater.* **35**, 405–415 (2023).
39. Chen, J. et al. Optoelectronic graded neurons for bioinspired in-sensor motion perception. *Nat. Nanotechnol.* **18**, 882–888 (2023).
40. Li, F. et al. An artificial visual neuron with multiplexed rate and time-to-first-spike coding. *Nat. Commun.* **15**, 3689 (2024).

Acknowledgements

This publication is based upon work supported by King Abdullah University of Science and Technology Research Funding (KRF) under Award No. ORA-2021-CRG10–4650, CRG10- 4668, CRG8-4095. W. Y. acknowledges the fundamental Research Funds for the Central Universities, Sun Yat-sen University (no. 23yxqntd002 and 24qnpy026). H. Ling acknowledges the Basic Research Program of Jiangsu (BK20240033). We acknowledge Iain McCulloch for providing us p(C_6NDI-T) from the University of Oxford, Department of Chemistry, Oxford, UK, and Xugang Guo for providing us f-BTI2TEG-FT from the Department of Materials Science and Engineering, Southern University of Science and Technology, Shenzhen, China.

Author contributions

Y. W. and W. S. contributed equally. S. I. conceived the research, designed the experiments, supervised the work, and wrote and edited the manuscript. Y. W. conceived the research, designed the experiments, synthesized the polymers, conducted OECT characterization and the characterization of photoelectrochemical synapse, graded neuron characterization, synaptic array for image recognition and memory, and wrote the manuscript. W. S. conducted the characterization of the optoelectrochemical synapse and performed UV-VIS-NIR spectrochemistry. H. Li conducted the simulation of graded neurons for motion, in-sensor reservoir computing, and color image processing, supervised by N. A. Y. Z. built a synaptic array for image recognition and memory. H. Ling conceived the graded neuron idea. J. U. evaluated the cytotoxicity of the polymer film. S. W. conducted the XPS and TEM characterization. T. C. conducted the CV and e-QCMD measurements. V. M. conducted TEM-cross section experiments. T. C. H. C. conducted the EIS measurement. W. Y. conducted GPC and GIWAXS measurements. All authors contributed to the discussion and writing.

Competing interests

The authors declare no competing interests.

Additional information

Supplementary information The online version contains supplementary material available at https://doi.org/10.1038/s41467-025-56814-w.

Correspondence and requests for materials should be addressed to Sahika Inal.

Peer review information *Nature Communications* thanks Gang Liu, Gunuk Wang, and the other, anonymous, reviewer(s) for their contribution to the peer review of this work. A peer review file is available.